

Inelastic $\text{H} + \text{H}_3^+$ Collision rates and their impact in the determination of the excitation temperature of H_3^+

Daniel Félix-González¹, Pablo del Mazo-Sevillano¹, Alfredo Aguado¹, Octavio Roncero², Jacques Le Bourlot^{3,4}, Evelyne Roueff³, Franck Le Petit³, and Emeric Bron³

¹ Unidad Asociada UAM-IFF-CSIC, Departamento de Química Física Aplicada, Facultad de Ciencias M-14, Universidad Autónoma de Madrid, 28049 Madrid (Spain)

² Instituto de Física Fundamental (IFF-CSIC), C.S.I.C., Serrano 123, 28006 Madrid, Spain. e-mail: octavio.roncero@csic.es

³ Sorbonne Université, Observatoire de Paris, Université PSL, CNRS, LERMA, 92190 Meudon, France

⁴ Université Paris-Cité

December 15, 2024

ABSTRACT

Context. In diffuse interstellar clouds the excitation temperature derived from the lowest levels of H_3^+ is systematically lower than that derived from H_2 . The differences may be attributed to the lack of state-specific formation and destruction rates of H_3^+ needed to thermalize the two species.

Aims. In this work, we want to check the role of rotational excitation collisions of H_3^+ with atomic hydrogen on its excitation temperature.

Methods. A time independent close-coupling method is used to calculate the state-to-state rate coefficients, using a very accurate and full dimensional potential energy surface recently developed for H_3^+ . A symmetric top approach is used to describe a frozen H_3^+ as equilateral triangle.

Results. Rotational excitation collision rate coefficients of H_3^+ with atomic Hydrogen have been derived in a temperature range appropriate to diffuse interstellar conditions up to $(J, K, \pm) = (7, 6, +)$ and $(J, K, \pm) = (6, 4, +)$ for its ortho and para forms. This allows to have a consistent set of collisional excitation rate coefficients and to improve the previous study where these contributions were speculated.

Conclusions. The new state-specific inelastic $\text{H}_3^+ + \text{H}$ rate coefficients yield differences up to 20% in the excitation temperature, and their impact increases with decreasing molecular fraction. We also confirm the impact of chemical state-to-state destruction reactions in the excitation balance of H_3^+ , and that reactive $\text{H} + \text{H}_3^+$ collisions are also needed to account for possible further ortho to para transitions.

Key words. Astrochemistry – ISM: abundances – ISM: molecules

1. Introduction

Hydrogen is the most abundant element in Universe and plays a key role in characterizing the physical conditions of the interstellar medium (ISM), the star formation and the chemical evolution of the molecular Universe (Oka 2013). Among its molecular forms (H_2 , H_2^+ and H_3^+), H_3^+ is an efficient protonator as the proton affinity of H_2 (422.3 kJ/mol) is smaller than that of most stable molecules (Watson 1973; Herbst & Klemperer 1973; Miller et al. 1989; Pagani et al. 1992; Tennyson 1995; McCall & Oka 2000; Oka 2012). For an atom or molecule (generally M) the reaction is:



The ionic hydrides thus formed trigger the chemistry cycles of many complex molecules in space (Watson 1973; Herbst & Klemperer 1973).

H_3^+ has been the subject of many review studies (Tennyson 1995; Herbst 2000; Oka 2012; Gerlich et al. 2012; Oka 2013; Miller et al. 2020) and special issues (Special issue 2012, 2019). Its infrared spectrum was first detected in the laboratory by Oka (1980) and later in space (Geballe & Oka 1989; Geballe et al. 1999; McCall et al. 1999; Oka 2013). Since then, H_3^+ has been

used to probe spatial conditions, as a thermometer and a clock of cold molecular clouds (Oka 2006; Pagani et al. 2011) and as a measure of the ionization rate of ISM (Le Petit et al. 2004; Indriolo & McCall 2012) and in the Central Molecular Zone of our Galaxy (Le Petit et al. 2016). Its infrared spectrum has been theoretically characterized with spectroscopic accuracy (Polyansky et al. 2012; Bachorz et al. 2009; Velilla et al. 2008; Tennyson et al. 2017; Furtenbacher et al. 2013), based on highly accurate potential energy surfaces (PESs) (Jaquet et al. 1998; Tennyson 1995; Cencek et al. 1998; Pavanello et al. 2012; Mizus et al. 2018; Bachorz et al. 2009; Velilla et al. 2010; Röhse et al. 1994; Viegas et al. 2007; Ghosh et al. 2017).

The absence of permanent dipole moment in the highly symmetric triangular equilibrium geometry in its ground vibrational state makes H_3^+ unobservable using pure rotational spectroscopy. H_3^+ is thus only observable through its vibrational spectrum. The recent availability of high sensitivity infrared observations thanks to the James Webb Spatial Telescope (JWST) has even allowed to detect infra red emission of H_3^+ in ultra luminous infra red galaxies (ULIRGs) (Pereira-Santaella et al. 2024). This opens the opportunity of a wider use of H_3^+ as a probe of the physical conditions of different objects in ISM.

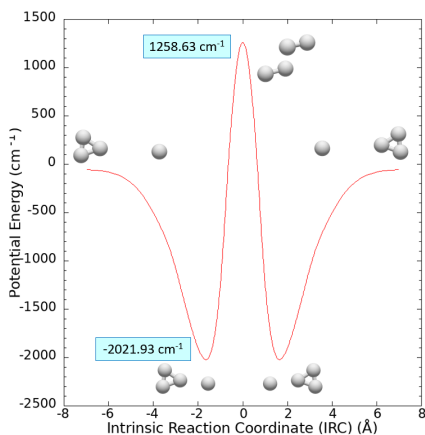


Fig. 1: Minimum energy path for the $\text{H} + \text{H}_3^+ \rightarrow \text{H}_3^+ + \text{H}$ exchange reaction for the PES by del Mazo-Sevillano et al. (2024)

The $\text{H}_3^+ + \text{H}_2$ collisional rates, including ortho/para transitions of the two species, have been reported in several theoretical studies (Oka & Epp 2004; Hugo et al. 2009; Park & Light 2007; Gómez-Carrasco et al. 2012). However the collisional rates with atomic hydrogen are yet non available despite their potential importance in partially molecular environments such as diffuse and translucent clouds and in the Central Molecular Zone of our Galaxy (Miller et al. 2020; Oka 2012).

The deuteration rates in $\text{D} + \text{H}_3^+$ and isotopic variants reactive collisions have been studied experimentally (Hillenbrand et al. 2019; Bowen et al. 2021). Due to the vibrational excitation in which H_3^+ is initially formed, a pure experimental determination of the deuteration rates is not possible. For this reason, a combined experimental and theoretical treatment has been used to determine the reactive deuteration rate constants. In such studies, tunneling through a potential barrier was estimated theoretically, but produced rate constants lower than $10^{-12} \text{ cm}^3 \text{ s}^{-1}$ below 100 K. Ring Polymer Molecular Dynamics calculations (Bulut et al. 2019), including quantum effects, on these reactions agree pretty well with these combined experiment/theoretical results (Hillenbrand et al. 2019; Bowen et al. 2021) above 200 K, but below this temperature there is no full consensus about the role of the tunneling rate. Using the tunnelling values reported by Bowen et al. (2021) as an upper limit, we can conclude that the reactive exchange rate is lower than $10^{-12} \text{ cm}^3 \text{ s}^{-1}$ below 100 K and $10^{-10} \text{ cm}^3 \text{ s}^{-1}$ below 300 K. Under this circumstance $\text{H} + \text{H}_3^+$ rotational inelastic collisions can then be considered as the dominant process below 100 K.

The exchange barrier is of approximately 1258 cm^{-1} , as shown in Fig. 1, according to a very accurate potential energy surface (PES) recently developed to study the $\text{H}_2 + \text{H}_2^+ \rightarrow \text{H}_3^+ + \text{H}$ reaction (del Mazo-Sevillano et al. 2024). The complete quantum treatment of inelastic and reactive dynamics, specially considering ortho/para permutation symmetry, is now-a-days inaffordable, and new methods need to be developed to address that problem. Before addressing the full exact treatment, in this work we study the $\text{H} + \text{H}_3^+$ rotational inelastic collisions at low temperatures, corresponding majoritarilly to energies below the top of the barrier, to determine its role in the excitation temperature of H_3^+ .

In diffuse interstellar clouds the excitation temperature $T_{12}(\text{H}_3^+)$ derived from the lowest two levels of H_3^+ is systematically lower than the gas kinetic temperature as derived from H_2 lowest levels $T_{01}(\text{H}_2)$. Le Bourlot et al. (2024, hereafter Paper I) give a thorough discussion of H_3^+ excitation mechanisms and

propose an explanation of this observational fact. $T_{12}(\text{H}_3^+)$ is defined by:

$$T_{12}(\text{H}_3^+) = E_{12} / \ln \left(\frac{g_2 x_1}{g_1 x_2} \right) \quad (2)$$

Where $E_{12} = 32.86 \text{ K}$ is the energy difference between both levels, $g_2/g_1 = 2$ and x_1 and x_2 are the populations of levels 1 and 2 respectively. This difference comes as a surprise as H_3^+ is formed in the region where H_2 dominates and the lowest levels of both species should be thermalized at the gas kinetic temperature. As in most lines of sight only these 2 lowest levels are observed, all interpretation of H_3^+ excitation rely on that single value.

Paper I shows that the difference arises from the fact that state-specific formation and destruction processes of H_3^+ must be accounted for when computing the molecule detailed balance steady state. In essence, a significant fraction of the formation reaction $\text{H}_2^+ + \text{H}_2$ exothermicity populates high lying levels of H_3^+ (del Mazo-Sevillano et al. 2024) favoring the para form at low temperature by nuclear spin selection rules (Oka 2004). These levels decay efficiently by radiative transitions to the lowest accessible level, which is either the para-(1, 1, -) level or the ortho-(3, 3, -) level (which is metastable). But the lower lying ortho-(1, 0, +) level can only be populated by slow reactive collisions, mainly with H_2 . This process comes into competition with destruction of the molecule by dissociative recombination with e^- , leading to an underpopulation of the lowest lying ortho level compared to a Boltzmann population at the gas kinetic temperature.

This mechanism is very sensitive to all the various state to state rates used. In the absence of better data, Paper I approximates collisions with H by taking H_2 rate coefficients scaled by a mass factor of $\sqrt{2}$. This was done for all transitions, including reactive ones. However, if reactive rate coefficients with H are negligible, this may lead to significant differences in a medium which is not fully molecular. Le Bourlot et al. (2024) also showed that possible small differences in the dissociative recombination rates of ortho and para modifications may have a significant impact on the excitation temperature.

In the following, the inelastic cross sections and rate constants are presented and discussed in Section 2 and their impact on two typical examples of diffuse lines of sight is presented in Section 3.

2. Inelastic Scattering Results

In this work we use the full dimensional PES developed by del Mazo-Sevillano et al. (2024), which considers all the degrees of freedom of the 4 atom systems very accurately using a Neural Network (NN) method (del Mazo-Sevillano et al. 2024). In addition, this PES describes very well the long-range interaction through the use of a triatom-in-molecules (TRIM) formalism (Sanz-Sanz et al. 2013, 2015), originally proposed for H_5^+ system (Aguado et al. 2010).

The $\text{H} + \text{H}_3^+$ inelastic rotational collisions are studied below 1500 cm^{-1} of translational energy, considering the rigid-rotor approach and the ortho/para symmetry of H_3^+ . To this aim we proceed in two steps. First, the triatomic levels of H_3^+ are calculated in full dimension, using permutationally invariant basis set functions represented in hyperspherical coordinates (Aguado et al. 2000; Sanz et al. 2001), as described in the Appendix A. Second, the inelastic rotational cross sections and rate constants are calculated using a close-coupling approach within a rigid rotor

approach, using a symmetric top + atom adapted from the study of NH₃ + He (Green 1980) and briefly described in Appendix B.

The resolution of the close-coupling equations is done as follows. A radial grid of 5000 equidistant points is used to describe R , from 1 to 100 bohr. In view of the energy requirements discussed for the basis selection (triatomic basis up to 4100 cm⁻¹), in this study we have considered 4000 equispaced total energies from 70 cm⁻¹ to 2070 cm⁻¹, with a step of 0.5 cm⁻¹, measured from the unphysical ground $A_1, J = 0, (0, 0^0)$ H₃⁺ level. The calculations are done up to a maximum total angular momentum $J = 30$, and separately for $\Gamma_t = A_2$ (ortho-H₃⁺) and E (para-H₃⁺) representations. The H₃⁺ states finally considered are shown in Fig. 2, for each irreducible representation Γ , and reducing the quantum numbers to $(j, \omega, p_t, \Gamma_t)$, which are the only needed in the scattering calculations presented below (see Appendix A).

Let us recall that the channels $\alpha \equiv (\beta, \ell)$ naturally arise from the triatomic levels $\beta \equiv (j, \omega, p_t, \Gamma_t)$ by introducing in each case all the allowed values for $\ell = |J - j|, \dots, J + j$. This implies that the number of channels rapidly increases with increasing the total angular momentum J . An additional truncation of channels is imposed. For triatomic levels above $j = 6$ (1200 cm⁻¹) within the $\Gamma_t = E$ representation, the simulated channels are constrained to $\ell \leq J + j/2$. This reduces the computation times, while the net effect on the final rate constants is small — note that most truncated channels are either predominantly closed or less contributing to the averages.

Transitions involving lower Δj , $\Delta\omega$, and $\Delta p_t = 0$ are expected to yield larger cross sections, simply because the radial potential coefficients, $V_{\lambda\nu}$ as defined in equation B.5, connecting them are larger for smaller λ and ν values, as can be seen in figure B.2.

It is expected that transitions involving fewer changes in the internal state of the system are more favored — *i.e.* higher $\sigma_{\beta\beta'}$ for lower Δj , $\Delta\omega$, and $\Delta p_t = 0$. From a mathematical point of view, the transition probability is maximized when the dominant radial coefficients $V_{\lambda\nu}$ in that transition are greater. By direct examination of figure B.2, it is clear that the coefficients are bigger in magnitude for smaller values of λ and ν , the latter being more critical — for example, $V_{\lambda=2, \nu=0}$ is comparable to $V_{\lambda=3, \nu=3}$. As long as $\nu = \Delta\omega$ and $\lambda \geq \Delta j$, the intuitive rules are completely equivalent to the rigorous mathematical criterion.

Apart from this rule, it is important to consider that the channels have an energy threshold. The radial coefficients of the dissociative wave function oscillate with a frequency proportional to $\sqrt{2\mu(E - E_{j\omega p_t})}$. Having closer thresholds implies similar frequencies, what maximizes the effective radial integrals, yielding larger transition probabilities.

For the $\Gamma_t = A_2$ representation (ortho-H₃⁺), we present in figure 3 the transitions starting from $(1, 0, +)$, the lowest level in this representation. In this representation, the ω quantum number for all the levels are positive integers multiple of three, and the transitions correspond to $\nu = \Delta\omega$ which are always multiples of three. In other words, all the transitions for this representation are symmetry allowed.

Starting from $(1, 0, +)$, the most favored transition would be to the $(3, 0, +)$ level, as it is energetically close to the entrance level and fulfils $\Delta\omega = 0, \Delta j = 2 [V_{\lambda=2, \nu=0}]$ and $\Delta p_t = 0$. In view of figure 3, this statement is apparently only true for higher energies, but at lower energies the transitions to $(3, 3, -)$ dominate, with $\Delta\omega = 3, \Delta j = 2 [V_{\lambda=3, \nu=3}]$ and $\Delta p_t \neq 0$. The coefficients $V_{\lambda=2, \nu=0}$ and $V_{\lambda=3, \nu=3}$ have a comparable magnitude, but the $(3, 3, -)$ level is closer in energy to the $(1, 0, +)$ entrance level. In such situation the energy criterion described above dominates.

A similar case occurs for the transitions to $(5, 0, +) [V_{\lambda=4, \nu=0}]$. For energies below its threshold other less favoured transitions have a higher probability than expected (such as $(5, 3, -) [V_{\lambda=5, \nu=3}]$). However, once the level opens, its transition probability rapidly increases and finally dominates over the former one.

For the $\Gamma_t = E$ representation (para-H₃⁺), the same propensity rules apply, but some slight details must be taken into consideration. This time, for each energy level there are two degenerate states associated to the $\pm\omega$ projections. For a generic transition between two levels β and β' (each containing two degenerate states $\pm\omega$ and $\pm\omega'$, respectively), four possible sub-transitions may occur. According to the selection rules, two of these sub-transitions are always forbidden, while the other two have exactly the same cross-section. As a consequence, the final average associated to that transition is in practice equivalent to taking just one of the allowed sub-transitions.

Additionally, as already stated by Bouhafs et al. (2017) for analogous systems, the triatomic levels for this representation have values of ω which are not multiples of three. As a consequence, not all the transitions will have values of $\nu = \Delta\omega$ that are multiples of three, so there will be some symmetry-forbidden transitions.

In view of figure 4, starting from $(1, \pm 1, -)$, the most favored transition would be to the $(2, \pm 2, +)$ level because of its energetic proximity and with $\Delta\omega = 3, \Delta j = 1 [V_{\lambda=3, \nu=3}]$, $\Delta p_t \neq 0$. Then, once the $(2, \pm 1, -)$ level opens, its transition becomes dominant as expected — $\Delta\omega = 0, \Delta j = 1 [V_{\lambda=1, \nu=0}]$, $\Delta p_t = 0$.

There is an interesting phenomenon associated to this symmetry representation, which can be exemplified by the transitions to $(3, \pm 2, +)$ and $(4, \pm 4, +)$. They both correspond to the element $V_{\lambda=3, \nu=3}$ — $\Delta\omega = 3, \Delta p_t \neq 0$, with $\Delta j = 2$ and $\Delta j = 3$, respectively. Therefore, considering their relative energies, one may expect the former level to be more favored, but as we examine figure 4 we see that $(4, \pm 4, +)$ is indeed the dominant transition. This is because, within $\Gamma_t = E$, there is an extra propensity rule in relation to the sign of ω . Transitions from $(1, \pm 1, -)$ to $(3, \pm 2, +)$ imply a change in the sign of ω , while $(4, \pm 4, +)$ leaves the sign unaltered.

This physical intuitive argument can be algebraically justified if we take special attention to the expression of the 3-j symbols appearing in the angular elements of the potential, Eq. B.6. For the transition to $(3, \pm 2, +)$, the 3-j element has a value of -0.189 , while for $(4, \pm 4, +)$ it is 0.333 . For this reason, the latter is significantly more favored.

The rate constants share general tendencies in terms of the relative dominance of the transitions and are shown in Figs. 5, for temperatures between 10 and 300 K, as representative results corresponding to the endothermic transitions starting from $(1, 0, +)$ and $(1, \pm 1, -)$ within the $\Gamma_t = A_2$ and $\Gamma_t = E$ representations.

The three parameters α, β and γ obtained from the fit of the results of Fig. 5 to an Arrhenius-type rate constant

$$k(T) = \alpha \left(\frac{T}{300} \right)^\beta \exp\left(\frac{-\gamma}{T} \right) \quad (3)$$

are listed in Table 1, where $k(T)$ is in cm³ s⁻¹ and the temperatures are in K.

Additionally, in the S.I. we provide a file containing the calculated state-to-state rate constants at some selected temperatures, for the de-excitation in this case, in the format required by the Meudon PDR code (Le Petit et al. 2006). This code computes the steady state of a 1D irradiated slab of interstellar gas

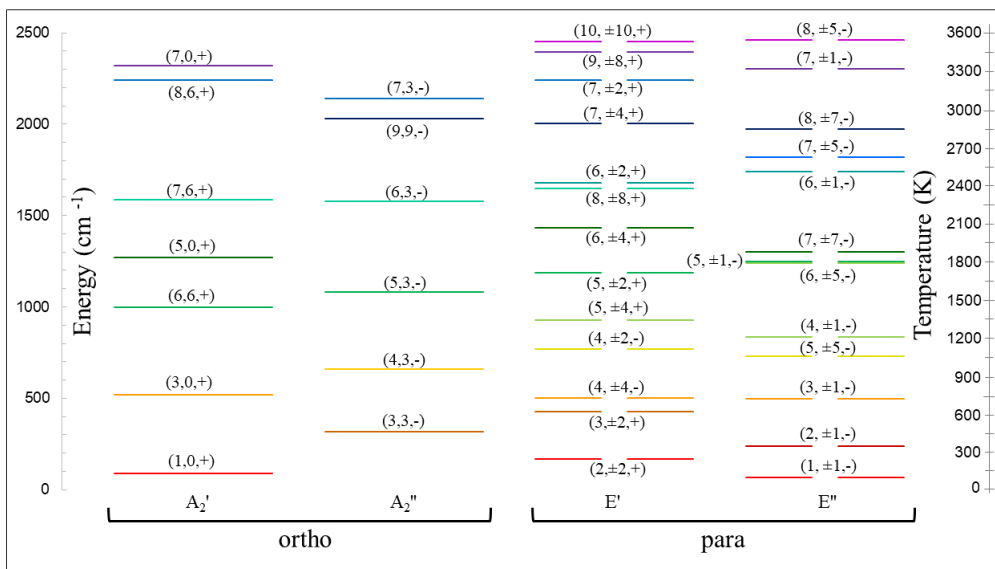


Fig. 2: Computed H_3^+ rotational levels in the ground vibrational state, conventionally labelled as (j, ω, p_l) within each specific irreducible representation, Γ .

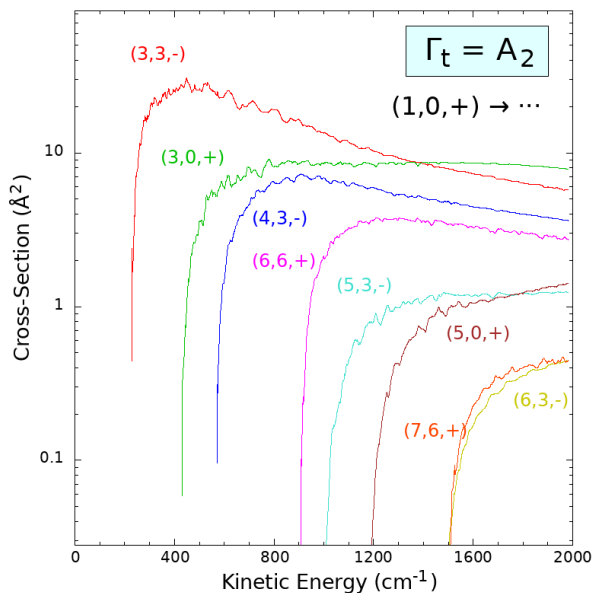


Fig. 3: Calculated cross-sections for the transitions starting from $(1,0,+) \rightarrow (j', \omega', p_l)$ within the $\Gamma_t = A_2$ representation.

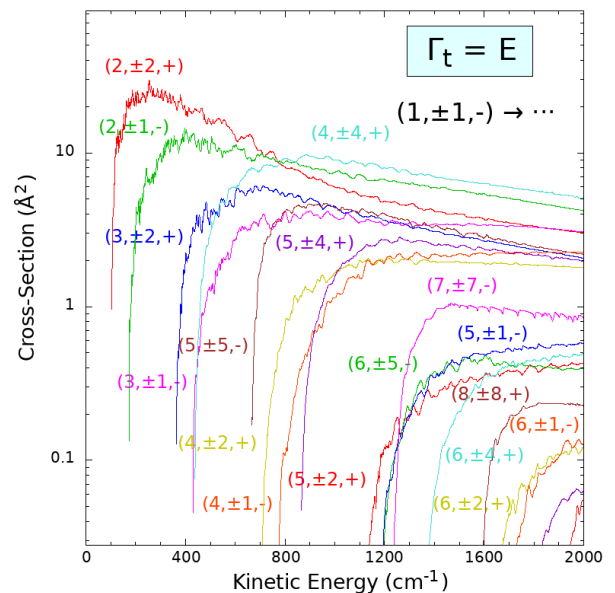


Fig. 4: Calculated cross-sections for the transitions starting from $(1,\pm 1,-)$ within the $\Gamma_t = E$ representation.

by solving for chemical, thermal balance, radiative transfer and statistical equilibrium of many observed species¹.

3. Observations and models

In Paper I, the authors discuss the excitation of H_3^+ towards 9 lines of sight (see their Table 2 and references therein). Here, we only consider two of them: HD 110432 and HD 73882. As shown in Table 2, which summarizes the main observational results, the former has a rather low molecular fraction defined as $2n(\text{H}_2)/(2n(\text{H}_2) + n(\text{H}))$ and warm kinetic temperature, while the latter is colder and has a higher molecular fraction. Here,

¹ Available at <https://pdr.obspm.fr>

$x_{obs}(\text{H}_3^+)$ is the ratio of the column densities of H_3^+ and H_2 , which is believed to be representative of the ion local fractional abundance, and f_{obs} is the molecular fraction towards the line of sight derived from data from Edenhofer et al. (2024) as found in Table 1 of Obolentseva et al. (2024). These values use results from the GAIA DR3 release which gives the repartition of absorbing matter along the line of sight towards nearby stars. The derived molecular fraction is larger than that obtained from the measured column densities of atomic and molecular Hydrogen from ultraviolet observations. That occurrence is due to the possible presence of atomic hydrogen on the line of sight that does not belong to the considered interstellar translucent cloud. The distances of HD110432 and HD73882 are respectively 438 pc and 461 pc (obtained from their measured parallax available on the

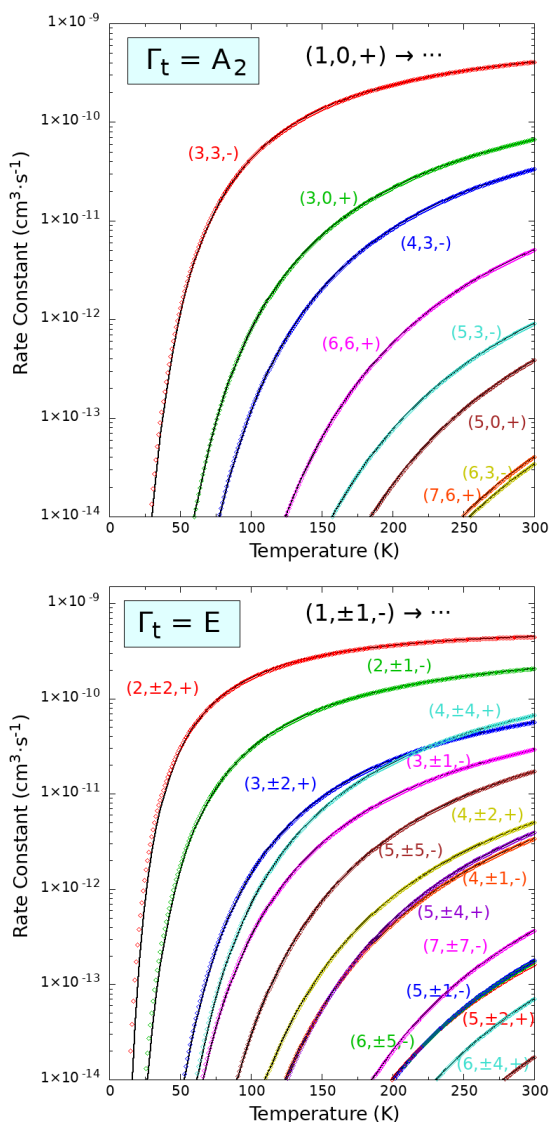


Fig. 5: Calculated state-to-state rate constants for the transitions starting from $(1,0,+)$ within the $\Gamma_t = A_2$ (top panel) and E (bottom panel) representations. The fitted curves are represented by the solid black lines, while the computed data are the coloured dots.

SIMBAD database), the sizes of the clouds are about a few pc, so that even a very small atomic hydrogen volumic density, located randomly on the line of sight, may contribute to the atomic column density by a non negligible amount.

Using the gas temperature deduced from H₂ excitation and the observed molecular fraction, we can use the code `ExcitH3+`² to test the impact of various rate coefficients on H₃⁺ excitation.

We compare the impact of the new rates of collision to the proxy used in Paper I: $k_H = \sqrt{2} k_{pH_2}$, where k_{pH_2} are the rate coefficients of H₃⁺ with para H₂, taken from Gómez-Carrasco et al. (2012). Figure 6 shows the rate coefficients for transitions between levels $(2, 2, +)$ and $(1, 1, -)$ (lowest para) and $(3, 3, -)$ and $(1, 0, +)$ (lowest ortho). We see that the new rates are stronger than the proxy, and that the values involving ortho transitions on one hand and para transitions on the other are much closer. Colli-

Table 1: Fitted parameters for the transitions $(j, \omega, p_i) \rightarrow (j', \omega', p_i', \Gamma_t)$ within $\Gamma_t = A_2$ $(1,0,+)$ and E $(1,\pm,-)$ representations.

(j', ω', p_i', A_2)	$\alpha \cdot 10^{10} (\text{cm}^3 \text{s}^{-1})$	β	$\gamma(K)$
(3,3,-)	14.599	-0.26	382.66
(3,0,+)	5.813	0.12	648.88
(4,3,-)	6.474	-0.22	887.95
(6,6,+)	5.323	-0.36	1395.86
(5,3,-)	1.659	-0.29	1560.41
(5,0,+)	1.936	-0.48	1864.97
(6,3,-)	0.871	-1.02	2352.99
(7,6,+)	1.004	-1.04	2345.26
(j', ω', p_i', E)	$\alpha \cdot 10^{10} (\text{cm}^3 \text{s}^{-1})$	β	$\gamma(K)$
(2,±2,+)	8.610	-0.28	196.07
(2,±1,-)	5.614	-0.06	300.40
(3,±2,+)	3.857	-0.15	576.62
(3,±1,-)	2.728	0.06	670.19
(4,±4,+)	6.615	-0.01	688.64
(5,±5,-)	5.190	-0.37	1020.62
(4,±2,+)	1.926	-0.04	1094.03
(4,±1,-)	2.01	0.06	1224.65
(5,±4,+)	3.486	-0.28	1344.99
(5,±2,+)	0.526	-0.32	1732.73
(6,±5,-)	0.839	-0.58	1856.99
(5,±1,-)	0.869	-0.46	1854.82
(7,±7,-)	0.220	-0.70	1917.51
(6,±4,+)	0.936	-0.77	2157.21

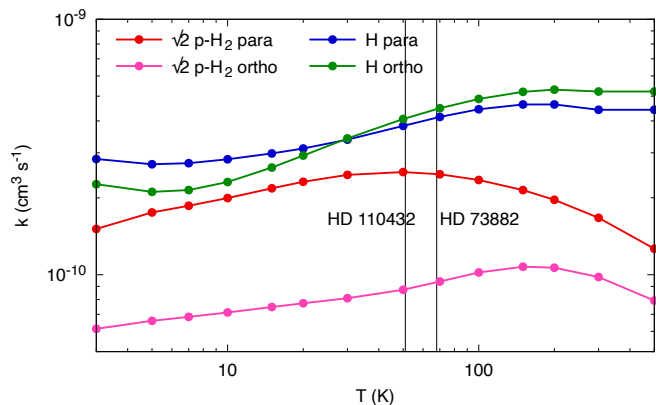


Fig. 6: Comparison of new H collision rate coefficients with the proxy used in Le Bourlot et al. (2024) for the lowest para and ortho transitions. The temperatures of HD 110432 and HD 73882, as derived from molecular hydrogen $J = 1$ and $J = 0$ column density ratio $T_{01}(\text{H}_2)$, are indicated by a black vertical line.

sions with electrons are included, using the results of Kokoouline et al. (2010).

Paper I emphasized the important role of H₃⁺ destruction rate k_{DR} that is due to dissociative recombination, for which the values pertaining to the para form, k_{DR}^p , and to the ortho form, k_{DR}^o , are introduced. As in Paper I, we adopt a standard electronic recombination rate of H₃⁺ with electrons of $k_{DR}^p(T) = 5.23 \cdot 10^{-8} \left(\frac{T}{300}\right)^{-0.75} \text{cm}^3 \text{s}^{-1}$. However, Paper I stresses that the exact rate is still not well known and, in particular, that ortho and para levels may have different rates. Pagani et al. (2009) suggests a constant rate of $k_{DR}^o = 6 \cdot 10^{-8} \text{cm}^3 \text{s}^{-1}$ below 250 K for ortho-H₃⁺ (see discussion in Section 3.3 of Paper I). So, for each

² Available at <https://excit3p.ism.obspm.fr>

Table 2: Observational data.

HD	E_{B-v} mag	A_v mag	$N(\text{H}_3^+)$ 10^{13} cm^{-2}	$N(\text{H}_2)$ 10^{20} cm^{-2}	$x_{\text{Obs}}(\text{H}_3^+)$ $\times 10^{-8}$	$T_{01}(\text{H}_2)$ K	$T_{12}(\text{H}_3^+)$ K	f_{Obs}
110432	0.40	2.02 ± 0.33	5.2	4.4	11.8	68	30	0.56
73882	0.72	2.36 ± 0.23	9.0	13.1	6.87	51	23	0.85

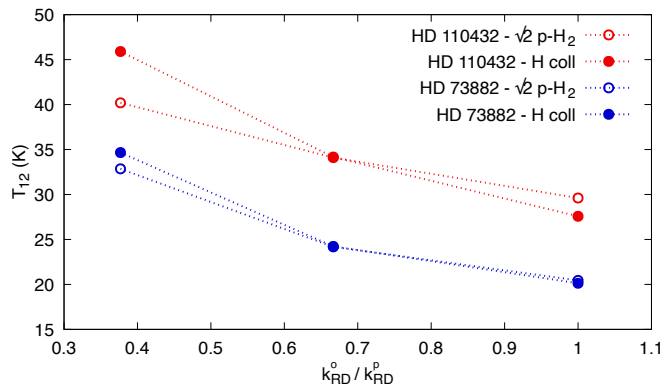


Fig. 7: Computed values of T_{12} for the two lines of sight and three ratios of k_{DR}^o/k_{DR}^p . Proxy: $k_H = \sqrt{2} k_{p\text{H}_2}$, H coll: k_H from this work.

line of sight we use three values of the ratio k_{DR}^o/k_{DR}^p (close to 1/3, 2/3 and 1), corresponding respectively to the rates of [Pagani et al. \(2009\)](#) at 60 K, an intermediate case and identical rate coefficients.

This leads to 6 different estimates of $T_{12}(\text{H}_3^+)$ for each line of sight (3 recombination rates for H_3^+ , times 2 sets of collision rate coefficients with H). They are presented on Figure 7.

We see that changing the ratio k_{DR}^o/k_{DR}^p has a strong impact on the computed value of $T_{12}(\text{H}_3^+)$. In addition, using the para- H_2 proxy leads to a reduced amplitude of the variations of $T_{12}(\text{H}_3^+)$ with k_{DR}^o . A particularly remarkable result is that, for a given line of sight, the $T_{12}(\text{H}_3^+)$ curves cross for an intermediate value of k_{DR}^o/k_{DR}^p . So, for that specific value only, there is no difference in the excitation temperature between the two sets of collision rate coefficients. As expected, the impact of the new rates is larger for lower values of the molecular fraction, as in HD 110432 compared to HD 73882.

Studying the origin of the sensitivity of $T_{12}(\text{H}_3^+)$ to k_{DR}^o/k_{DR}^p is out of the scope of this work, and will be done in another paper. However, regardless of the final determination of the recombination rates, it remains essential to use the new collision rate coefficients with H, as they result in significantly different evaluations of $T_{12}(\text{H}_3^+)$. Depending on the line of sight considered and the choice of other physical parameters, the differences may reach up to 20% compared to using the proxy.

4. Conclusions

In this paper we introduce new accurate computations of collisional cross sections and collisional rate coefficients of H_3^+ with H for energies adapted to the physical conditions in the Interstellar Medium.

A time independent close-coupling method is used to calculate the state-to-state cross sections and rate coefficients, using a very accurate and full dimensional potential energy surface

recently developed for this system ([del Mazo-Sevillano et al. 2024](#)). H_3^+ rovibrational levels are calculated using hyperspherical coordinates, in permutationally symmetry adapted functions up to $j = 20$ and including the vibrations. From all these levels, only those corresponding to the ground $(0,0^0)$ vibrational state are selected and included in the close-coupling method in a symmetric top approach, considering frozen H_3^+ as equilateral triangle but with the numerically exact energy levels obtained in full-dimensional H_3^+ rovibrational states.

We use these new rate coefficients to evaluate the excitation temperature of H_3^+ as determined from its 2 lowest levels. Compared to using a proxy based on para H_2 , we find that:

- Differences in the estimated excitation temperature may reach 20%.
- The impact of the new rate coefficients increases as the cloud molecular fraction decreases.
- Differences between electronic recombination rates of ortho and para H_3^+ have a significant impact on the estimated excitation temperature, with differences larger with the new H collision rates.

This later point leads to large difficulties in estimating physical conditions from the observed values of H_3^+ abundance and excitation. The reasons for this sensitivity will be explored in a future paper, but it stresses the necessity to still improve our understanding of this long standing question.

In the present work, no estimation is done of possible reactive collisions between H and H_3^+ that may lead to ortho to para transitions. Inspection of the PES shows that these rates must be low (lower than $10^{-12} \text{ cm}^3 \text{ s}^{-1}$ below 100 K), but even a low value may have an impact in some specific conditions, and that question too deserves further examination.

As a last point, the present work does not include radiative pumping in the infrared range, which is invoked in [Pereira-Santaella et al. \(2024\)](#) to explain their observations of vibrationally excited H_3^+ in (U)LIRGs.

5. Data availability

The energy levels of H_3^+ obtained in this work are listed in file [H3p-levels-exomol.dat](#).

The inelastic rates of ortho and para symmetries are provided in the files [A2-rates.dat](#) and [E-rates.dat](#) files, respectively.

Acknowledgements. The research leading to these results has received funding from MICIN (Spain), under grant PID2021-122549NB-C21 and PID2021-122549NB-C22, and by the Programme National « Physique et Chimie du Milieu Interstellaire » (PCMI) of the CNRS/INSU with INC/INP co-funded by CEA and CNES. Computational assistance was provided by the Supercomputer facilities of Lusitania founded by the CénitS and Computaex Foundation.

References

Abramowitz, M. & Stegun, I. 1972, Handbook of mathematical functions (Dover Publications, Inc., New York)

- Aguado, A., Barragan, P., Prosmi, R., et al. 2010, *J. Chem. Phys.*, 133, 024306
- Aguado, A., Roncero, O., Tablero, C., Sanz, C., & Paniagua, M. 2000, *J. Chem. Phys.*, 112, 1240
- Arthurs, A. M. & Dalgarno, A. 1960, *Proc. R. Soc. Lond. A Math. Phys. Sci.*, 256, 540
- Bachorz, R. A., Cencek, W., Jaquet, R., & Komasa, J. 2009, *The Journal of chemical physics*, 131, 024105
- Bouhaf, N., Rist, C., Daniel, F., et al. 2017, *Mon. Not. R. Astronom. Soc.*, 470, 2204
- Bowen, K. P., Hillenbrand, P.-M., Liévin, J., Savin, D. W., & Urbain, X. 2021, *J. Chem. Phys.*, 154, 084307
- Bulut, N., Aguado, A., Sanz-Sanz, C., & Roncero, O. 2019, *J. Phys. Chem. A*, 123, 8766
- Cencek, W., Rychlewski, J., Jaquet, R., & Kutzelnigg, W. 1998, *J. Chem. Phys.*, 108, 2831
- Cullum, J. & Willoughby, R. 1985, *Lanczos Algorithms for Large Symmetric Eigenvalues Computations* (Birkhäuser, Boston)
- del Mazo-Sevillano, P., Félix-González, D., Aguado, A., et al. 2024, *Mol. Phys.*, e2183071
- Edenhofer, G., Zucker, C., Frank, P., et al. 2024, *A&A*, 685, A82
- Fröberg, C.-E. 1985, *Numerical Mathematics: Theory and Computer Applications* (The Benjamin/Cummings Publishing Company)
- Furtenbacher, T., Szidarovsky, T., Matyus, E., Fabri, C., & Csaszar, A. G. 2013, *Journal of Chemical Theory and Computation*, 9, 5471
- Gadéa, F. X., Berriche, H., Roncero, O., Villarreal, P., & Delgado-Barrio, G. 1997, *J. Chem. Phys.*, 107, 10515
- Geballe, T. R., McCall, B. J., Hinkle, K. H., & Oka, T. 1999, *AstroPhys. J.*, 510, 251
- Geballe, T. R. & Oka, T. 1989, *AstroPhys. J.*, 342, 855
- Gerlich, D., Jusko, P., Š. Roučka, et al. 2012, *Ap. J.*, 749, 22
- Ghosh, S., Mukherjee, S., Mukherjee, B., et al. 2017, *J. Chem. Phys.*, 147, 074105
- Gómez-Carrasco, S., González-Sánchez, L., Aguado, A., Zanchet, A., & Roncero, O. 2012, *J. Chem. Phys.*, 137, 094303
- Green, S. 1976, *J. Chem. Phys.*, 64, 3463
- Green, S. 1980, *J. Chem. Phys.*, 73, 2740
- Herbst, E. 2000, *Phil. Trans. R. Soc. Lond. A*, 358, 2523
- Herbst, E. & Klemperer, W. 1973, *Astrophys. J.*, 185, 505
- Hillenbrand, P.-M., Bowen, K. P., Liévin, J., Urbain, X., & Savin, D. W. 2019, *Astrophys. J.*, 877, 38
- Hugo, E., Asvany, O., & Schlemmer, S. 2009, *J. Chem. Phys.*, 130, 164302
- Indriolo, N. & McCall, B. J. 2012, *ApJ*, 745, 91
- Jaquet, R., Cencek, W., Kutzelnigg, W., & Rychlewski, J. 1998, *J. Chem. Phys.*, 108, 2837
- Kokoouline, V., Faure, A., Tennyson, J., Greene, C. H. 2010, *MNRAS*, 405, 1195
- Le Bourlot, J., Roueff, E., Le Petit, F., et al. 2024, *Molecular Physics*, 122, e2182612
- Le Petit, F., Nehmé, C., Le Bourlot, J., & Roueff, E. 2006, *ApJS*, 164, 506
- Le Petit, F., Roueff, E., & Herbst, E. 2004, *A&A*, 417, 993
- Le Petit, F., Ruaud, M., Bron, E., et al. 2016, *Astron. Astrophysics.*, 585, A105
- McCall, B. J., Geballe, T. R., Hinkle, K. H., & Oka, T. 1999, *AstroPhys. J.*, 522, 338
- McCall, B. J. & Oka, T. 2000, *Science*, 287, 1941
- Millar, T. J., Bernett, A., & Herbst, E. 1989, *Astrophys. J.*, 340, 906
- Miller, S., Tennyson, J., Geballe, T. R., & Stallard, T. 2020, *Rev. Mod. Phys.*, 92, 035003
- Mizus, I. I., Polyansky, O. L., McKemmish, L. K., et al. 2018, *Molecular Physics*, 117, 1663
- Obolentseva, M., Ivlev, A. V., Silsbee, K., et al. 2024, *arXiv e-prints*, [arXiv:2408.11511](https://arxiv.org/abs/2408.11511)
- Oka, T. 1980, *Phys. Rev. Lett.*, 45, 531
- Oka, T. 2004, *J. Mol. Spectros.*, 228, 635
- Oka, T. 2006, *PNAS*, 103, 12235
- Oka, T. 2012, *Phil. Trans. R. Soc. A*, 370, 4991
- Oka, T. 2013, *Chem. Rev.*, 113, 8738
- Oka, T. & Epp, E. 2004, *Astrophys. J.*, 613, 349
- Pack, R. T. & Parker, G. A. 1989, *J. Chem. Phys.*, 90, 3511
- Pagani, L., Roueff, E., & Lesaffre, P. 2011, *Astrophys. J. Lett.*, 739, L35
- Pagani, L., Salez, M., & Wannier, P. 1992, *Astron. Astrophys.*, 258, 479
- Pagani, L., Vastel, C., Hugo, E., et al. 2009, *Astronomy and Astrophys.*, 494, 623
- Park, K. & Light, J. C. 2007, *J. Chem. Phys.*, 126, 044305
- Pavanello, M., Adamowicz, L., Aljiah, A., et al. 2012, *J Chem Phys*, 136, 184303
- Pereira-Santaella, M., González-Alfonso, E., García-Bernete, I., et al. 2024, *A&A*, 689, L12
- Polyansky, O. L., Aljiah, A., Zobov, N. F., et al. 2012, *Philos Trans A Math Phys Eng Sci*, 370, 5014
- Röhse, R., Kutzelnigg, W., Jaquet, R., & Klopper, W. 1994, *The Journal of chemical physics*, 101, 2231
- Sanz, C., Roncero, O., Tablero, C., Aguado, A., & Paniagua, M. 2001, *J. Chem. Phys.*, 114, 2182
- Sanz-Sanz, C., Aguado, A., Roncero, O., & Naumkin, F. 2015, *J. Chem. Phys.*, 143, 234303
- Sanz-Sanz, C., Roncero, O., Paniagua, M., & Aguado, A. 2013, *J. Chem. Phys.*, 139, 184302
- Special issue. 2012, *Phil. Trans. R. Soc. A*, 370
- Special issue. 2019, *Phil. Trans. R. Soc. A*, 377
- Tennyson, J. 1995, *Rep. Prog. Phys.*, 58, 412
- Tennyson, J., Polyansky, O. L., Zobov, N. F., Aljiah, A., & Császár, A. G. 2017, *J. Phys. B: At. Mol. Opt. Phys.*, 50, 232001
- Velilla, L., Lepetit, B., Aguado, A., Beswick, J. A., & Paniagua, M. 2008, *J. Chem. Phys.*, 129, 084307
- Velilla, L., Paniagua, M., & Aguado, A. 2010, *International Journal of Quantum Chemistry*, 111, 387
- Viegas, L. P., Aljiah, A., & Varandas, A. J. C. 2007, *J Chem Phys*, 126, 074309
- Watson, J. 1984, *J. Mole. Spect.*, 103, 350
- Watson, W. D. 1973, *Astrophys. J.*, 183, L17
- Zare, R. 1988, *Angular Momentum* (John Wiley and Sons, Inc.)

Appendix A: H_3^+ levels

For the H_3^+ we use the PES for H_4^+ of [del Mazo-Sevillano et al. \(2024\)](#), placing the fourth hydrogen atom at 100 bohr at a fixed geometry. The rovibrational bound states of H_3^+ are calculated in the adiabatically adjusting, Johnson's principal axis, hyperspherical (denoted APJH) coordinates ([Pack & Parker 1989](#)) using a code previously developed ([Aguado et al. 2000](#); [Sanz et al. 2001](#)), in which the full wave function is expanded as

$$\Psi_i^{jm\Gamma}(\rho, \theta, \phi_\tau, \alpha, \beta, \gamma) = 4\rho^{-5/2} \sum_{v,k,n,\Omega} C_{v,k,n,\Omega}^{jm\Gamma} \times \tilde{W}_{\Omega,n}^{jm\Gamma}(\alpha, \beta, \gamma, \phi_\tau) F_k^{j,\Omega,n}(\theta) \varphi_v(\rho), \quad (\text{A.1})$$

where, $\varphi_v(\rho)$ are numerical functions obtained in a mono-dimensional radial grid in ρ for the equilibrium configuration ([Aguado et al. 2000](#)), $F_k^{j,\Omega,n}(\theta)$ are proportional to Jacobi polynomials ([Aguado et al. 2000](#); [Abramowitz & Stegun 1972](#)) and $\tilde{W}_{\Omega,n}^{jm\Gamma}(\alpha, \beta, \gamma, \phi_\tau)$ are symmetry adapted basis set functions for a given triatomic angular momentum j , with projection m on the space fixed frame and an irreducible representation, Γ , of the D_{3h} point group (isomorphic with the S_3 permutation group multiplied by the inversion of spatial symmetry). These symmetry adapted functions are expressed as

$$\tilde{W}_{\Omega,n}^{jm\Gamma}(\alpha, \beta, \gamma, \phi_\tau) = A_{\Omega,n}^{j\Gamma} W_{\Omega,n}^{jm}(\alpha, \beta, \gamma, \phi_\tau) + B_{\Omega,n}^{j\Gamma} W_{-\Omega,-n}^{jm}(\alpha, \beta, \gamma, \phi_\tau), \quad (\text{A.2})$$

where $A_{\Omega,n}^{j\Gamma}$ and $B_{\Omega,n}^{j\Gamma}$ coefficients are obtained applying projection operators ([Aguado et al. 2000](#); [Sanz et al. 2001](#)), and

$$W_{n\omega}^{jm}(\alpha, \beta, \gamma, \phi_\tau) = \sqrt{\frac{2j+1}{8\pi^2}} D_{m\omega}^{j*}(\alpha, \beta, \gamma) \frac{e^{in\phi_\tau}}{\sqrt{2\pi}}, \quad (\text{A.3})$$

with $D_{m\omega}^{j*}(\alpha, \beta, \gamma)$ being Wigner rotation functions ([Zare 1988](#)), transforming from the space fixed to the body-fixed frame, with the axes along the principal inertia axes and the z-axis perpendicular to the plane of H_3^+ , with ω being the projection of the triatomic total angular momentum in the body-fixed z-axis.

The exact triatomic eigenvalues and eigenvectors are obtained for each j, Γ values using a two steps method ([Aguado et al. 2000](#)). The eigenvalues are obtained using a non-orthogonal Lanczos method ([Cullum & Willoughby 1985](#)) and then the eigenfunctions are obtained using a conjugate gradient method ([Fröberg 1985](#)). From the eigenvectors the approximated quantum numbers (v_1, v_2^l) ([Watson 1984](#)) are obtained together with the ω distribution in Eq. A.1. Bound state calculations have been done up to $j = 15$ for ortho- H_3^+ (nuclear spin $I = 3/2$ and $\Gamma = A_2', A_2''$) and para- H_3^+ ($I = 1/2$, $\Gamma = E', E''$), which are listed in the Supplementary Information (S.I.) with the quantum numbers.

A.1. Simplifying to rigid rotor H_3^+

The scattering is treated in the rigid rotor approach, and not all the bound states are used. In what follows, we shall consider $\Gamma = \Gamma_t \times p_t$, to treat separately the permutation symmetry, Γ_t which is conserved in inelastic collisions, and the inversion of spacial coordinates, p_t , which is not conserved ($p_t=1$ for A_2' and E' , $p_t=-1$ for A_2'' and E''). To include the "exact" triatomic bound states in the scattering calculations described below, the following approximations have been done:

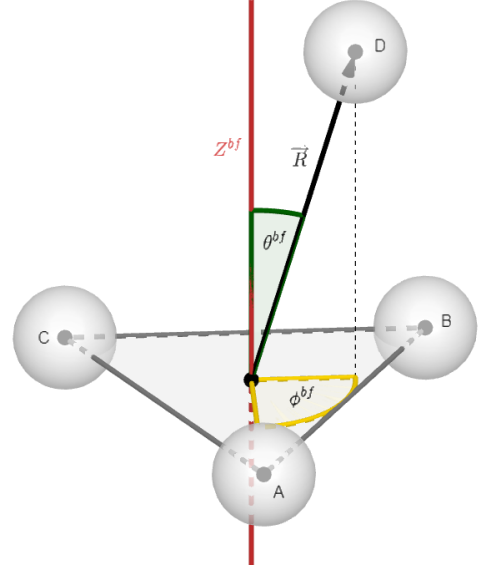


Fig. B.1: Relative orientation between both fragments, in a body-fixed frame centered in the triatom.

1. Only states corresponding to the ground vibrational level, $(0, 0^0)$, are included, up to an energy of 4100 cm^{-1} above the ground state.
2. Triatomic systems are in general asymmetric top. However, for the triangular equilibrium distance, H_3^+ is a symmetric top. In the exact bound calculations, the states in general are a linear superposition of several ω values, but for $(0, 0^0)$ and low triatomic angular momenta j there is a dominant ω value, with a weight larger than 90% (see S.I.). Thus, in the present case we shall consider H_3^+ as a symmetric top in the collisions studied below.
3. Under this symmetric top rigid-rotor approximation, bound states of Eq. A.1 are taken as

$$|jm\omega p_t \Gamma_t\rangle \equiv \sqrt{\frac{2j+1}{8\pi^2}} D_{m\omega}^{j*}(\alpha, \beta, \gamma), \quad (\text{A.4})$$

with the only restriction of adding an intrinsic parity under inversion of spatial coordinates, so that the parity of these functions coincide with the corresponding parity of the exact triatomic state, p_t . The functions thus defined have the proper permutation symmetry, A_2 or E in the present case.

4. For $\Gamma = E'$ or E'' , the functions $\tilde{W}_{n\omega}^{jm\Gamma} = f(W_{n\omega}^{jm\Gamma}, W_{-n-\omega}^{jm\Gamma})$ are decoupled from $\tilde{W}_{n-\omega}^{jm\Gamma} = f(W_{n-\omega}^{jm\Gamma}, W_{-n\omega}^{jm\Gamma})$, with n, ω different from zero. Thus, the two degenerate eigenstates are expressed in the corresponding basis functions separately, and labeled by ω and $-\omega$.

Appendix B: Inelastic scattering method

The inelastic scattering calculations have been performed with the code DTICC which has been specifically developed by the authors for this purpose, in which the close coupled equations are solved with a renormalized Numerov algorithm ([Gadéa et al. 1997](#)). The system composed by a symmetric top colliding with an atom is described in space fixed (SF) coordinates, using a standard method adapted from NH_3 ([Green 1980](#)), outlined here for completeness.

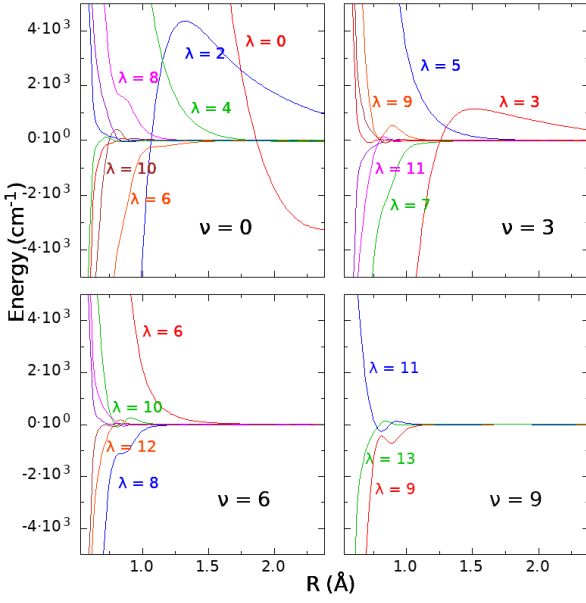


Fig. B.2: Radial coefficients corresponding to the expansion of the interaction potential.

A Jacobi vector $\mathbf{R} \equiv \{R, \theta_R, \phi_R\}$ is defined in the SF frame joining the ABC (or symmetric top) center-of mass to the colliding atom D, whose associated angular momentum is ℓ . The space-fixed angular basis set functions are defined as

$$|\alpha\rangle = \sum_{mm_\ell} \langle jm_\ell m_\ell | JM \rangle |jm\omega p_t \Gamma_t\rangle Y_{\ell m_\ell}(\theta_R, \phi_R), \quad (\text{B.1})$$

with $|jm\omega p_t \Gamma_t\rangle$ being defined in Eq. A.4. The $|\alpha\rangle = \mathcal{Y}_{j\omega p_t \Gamma_t}^{JM}(\alpha, \beta, \gamma, \theta_R, \phi_R)$ is introduced to simplify the notation. In this basis, the total scattering wave function is expressed as

$$|\Psi_E^{JM\alpha-}\rangle = \sum_{\alpha'} \frac{\Phi_{\alpha'}^{JM\alpha-}(R; E)}{R} |\alpha'\rangle \quad (\text{B.2})$$

where the radial coefficients $\Phi_{\alpha'}^{JM\alpha-}(R; E)$ are obtained numerically by solving the close coupled differential equations obtained by inserting this total wave function, with the Hamiltonian being defined as

$$\hat{H} = -\frac{\hbar^2}{2\mu} \left(\frac{2}{R} \frac{\partial}{\partial R} + \frac{\partial^2}{\partial R^2} \right) + \frac{\hat{\ell}^2}{2\mu R^2} + V(R, \theta^{bf}, \phi^{bf}) + \hat{H}_{ABC} \quad (\text{B.3})$$

where $\mu = m_D m_{ABC} / (m_D + m_{ABC})$ is the reduced mass, \hat{H}_{ABC} is the internal triatomic hamiltonian operator, and $V(R, \theta^{bf}, \phi^{bf})$ is the interaction potential which only depends on the relative orientation of the atom D with respect to the triatomic fragment ABC — as shown in Fig. B.1.

The centrifugal term $\hat{\ell}^2$ is diagonal in the SF representation with eigenvalues $\hbar^2 \ell(\ell + 1)$. The eigenstates and eigenvalues of the ABC system were obtained in the previous section, which in the present treatment are simplified to the symmetry adapted symmetric top functions, $|jm\omega p_t \Gamma_t\rangle$. The potential matrix elements in the space-fixed representation are then given by

$$\langle \alpha | V | \alpha' \rangle = \sum_{\lambda\nu} V_{\lambda\nu}(R) \langle \alpha | Y_{\lambda\nu} | \alpha' \rangle, \quad (\text{B.4})$$

where $V_{\lambda\nu}(R)$ are the radial coefficients of the expansion of the potential in spherical harmonics as

$$V(R, \theta^{bf}, \phi^{bf}) = \sum_{\lambda\nu} V_{\lambda\nu}(R) Y_{\lambda\nu}(\theta^{bf}, \phi^{bf}), \quad (\text{B.5})$$

which are shown in Fig. B.2, and

$$\langle \alpha | Y_{\lambda\nu} | \alpha' \rangle = \sqrt{\frac{[\ell][\lambda][\ell'][\lambda']}{4\pi}} (-1)^{-J+\lambda-\omega'} \begin{pmatrix} \ell & \lambda & \ell' \\ 0 & 0 & 0 \end{pmatrix} \begin{pmatrix} j & J & \ell \\ \ell' & \lambda & j' \end{pmatrix} \begin{pmatrix} j & \lambda & j' \\ \omega & \nu & -\omega' \end{pmatrix}, \quad (\text{B.6})$$

where the compact notation $[j] = 2j + 1$ has been used for the angular momenta degeneracies, and the 6-j symbols (Zare 1988) are denoted as $\{ : : \}$. The symmetry of the potential ensures that the radial expansion coefficients fulfill the condition $V_{\lambda\nu}(R) = (-1)^\nu V_{\lambda-\nu}(R)$, as well as the threefold symmetry for the azimuthal angle $V(R, \theta^{bf}, \phi^{bf}) = V(R, \theta^{bf}, \phi^{bf} + 2n\pi/3)$ for $n \in \mathbb{Z}$. These symmetry constraints are equivalent to say that the only allowed values for ν are multiples of three: $\nu = 0, \pm 3, \pm 6, \dots$. The total parity of the four atom system is conserved and equal to $p = p_t(-1)^\ell$, so that $p_t = \pm 1$ is no longer conserved.

As noted above, the symmetry adapted rigid rotor wave functions of H₃⁺ used in this work constitute a slight modification, essentially equivalent, of the usual treatment for collisions of symmetric top functions with atoms (Green 1976, 1980). First, the procedure followed allows to exactly determine the symmetry of the triatomic function, which also depends on the hyperspherical angle ϕ_τ , which is not included in the rigid rotor approach.

The state-to-state cross section are obtained using the usual partial wave summation in the space fixed frame (Arthurs & Dalgarno 1960) as

$$\sigma_{\beta\beta'}^{\Gamma_t}(E) = \frac{\pi}{(2j+1)k_\beta^2} \sum_{J\ell\ell'p} (2J+1) |S_{\alpha\alpha'}^{J\Gamma_t p}(E) - \delta_{\alpha\alpha'}|^2 \quad (\text{B.7})$$

where $k_\beta^2 = 2\mu(E - E_\beta)/\hbar^2$, E is the total energy, and E_β is the energy of the triatomic level β . $S_{\alpha\alpha'}^{J\Gamma_t p}(E)$ are the elements of the scattering matrices obtained in the resolution of the close coupling equations.

The state-to-state rate constants are obtained by taking Boltzmann averages on the cross-sections — *i.e.* integration over the kinetic energy $E_\beta^k = E - E_\beta$ for a given temperature T , as

$$k_{\beta\beta'}(T) = \sqrt{\frac{8}{\pi\mu(k_B T)^3}} \times \int dE_\beta^k E_\beta^k \sigma_{\beta\beta'}(E_\beta^k) e^{-\frac{E_\beta^k}{k_B T}} \quad (\text{B.8})$$

being k_B the Boltzmann constant.